

# Measurement of the Double-Beta Decay Half-Life and Search for the Neutrinoless Double-Beta Decay of $^{48}\text{Ca}$ with the NEMO-3 Detector

R. Arnold,<sup>1</sup> C. Augier,<sup>2</sup> A.M. Bakalyarov,<sup>3</sup> J.D. Baker,<sup>4,\*</sup> A.S. Barabash,<sup>5</sup> A. Basharina-Freshville,<sup>6</sup> S. Blondel,<sup>2</sup> S. Blot,<sup>7</sup> M. Bongrand,<sup>2</sup> V. Brudanin,<sup>8,9</sup> J. Busto,<sup>10</sup> A.J. Caffrey,<sup>4</sup> S. Calvez,<sup>2</sup> M. Cascella,<sup>6</sup> C. Cerna,<sup>11</sup> J.P. Cesar,<sup>12</sup> A. Chapon,<sup>13</sup> E. Chauveau,<sup>7</sup> A. Chopra,<sup>6</sup> D. Duchesneau,<sup>14</sup> D. Durand,<sup>13</sup> V. Egorov,<sup>8</sup> G. Eurin,<sup>2,6</sup> J.J. Evans,<sup>7</sup> L. Fajt,<sup>15</sup> D. Filosofov,<sup>8</sup> R. Flack,<sup>6</sup> X. Garrido,<sup>2</sup> H. Gómez,<sup>2</sup> B. Guillon,<sup>13</sup> P. Guzowski,<sup>7</sup> R. Hodák,<sup>15</sup> A. Huber,<sup>11</sup> P. Hubert,<sup>11</sup> C. Hugon,<sup>11</sup> S. Jullian,<sup>2</sup> A. Klimenko,<sup>8</sup> O. Kochetov,<sup>8</sup> S.I. Konovalov,<sup>5</sup> V. Kovalenko,<sup>8</sup> D. Lalanne,<sup>2</sup> K. Lang,<sup>12</sup> V.I. Lebedev,<sup>3</sup> Y. Lemièrre,<sup>13</sup> T. Le Noblet,<sup>14</sup> Z. Liptak,<sup>12</sup> X. R. Liu,<sup>6</sup> P. Loaiza,<sup>2</sup> G. Lutter,<sup>11</sup> F. Mamedov,<sup>15</sup> C. Marquet,<sup>11</sup> F. Mauger,<sup>13</sup> B. Morgan,<sup>16</sup> J. Mott,<sup>6</sup> I. Nemchenok,<sup>8</sup> M. Nomachi,<sup>17</sup> F. Nova,<sup>12</sup> F. Nowacki,<sup>1</sup> H. Ohsumi,<sup>18</sup> R.B. Pahlka,<sup>12</sup> F. Perrot,<sup>11</sup> F. Piquemal,<sup>11,19</sup> P. Povinec,<sup>20</sup> P. Přidal,<sup>15</sup> Y.A. Ramachers,<sup>16</sup> A. Remoto,<sup>14</sup> J.L. Reyss,<sup>21</sup> B. Richards,<sup>6</sup> C.L. Riddle,<sup>4</sup> E. Rukhadze,<sup>15</sup> N.I. Rukhadze,<sup>8</sup> R. Saakyan,<sup>6</sup> R. Salazar,<sup>12</sup> X. Sarazin,<sup>2</sup> Yu. Shitov,<sup>8,22</sup> L. Simard,<sup>2,23</sup> F. Šimkovic,<sup>20</sup> A. Smetana,<sup>15</sup> K. Smolek,<sup>15</sup> A. Smolnikov,<sup>8</sup> S. Söldner-Rembold,<sup>7</sup> B. Soulé,<sup>11</sup> I. Štekl,<sup>15</sup> J. Suhonen,<sup>24</sup> C.S. Sutton,<sup>25</sup> G. Szklarz,<sup>2</sup> J. Thomas,<sup>6</sup> V. Timkin,<sup>8</sup> S. Torre,<sup>6</sup> V.I. Tretyak,<sup>26</sup> V.I. Tretyak,<sup>8</sup> V.I. Umatov,<sup>5</sup> I. Vanushin,<sup>5</sup> C. Vilela,<sup>6</sup> V. Vorobel,<sup>27</sup> D. Waters,<sup>6</sup> S.V. Zhukov,<sup>3</sup> and A. Žukauskas<sup>27</sup>  
(NEMO-3 Collaboration)

<sup>1</sup>*IPHC, ULP, CNRS/IN2P3, F-67037 Strasbourg, France*

<sup>2</sup>*LAL, Université Paris-Sud, CNRS/IN2P3, Université Paris-Saclay, F-91405 Orsay, France*

<sup>3</sup>*NRC “Kurchatov Institute”, KI, 123182 Moscow, Russia*

<sup>4</sup>*Idaho National Laboratory, Idaho Falls, ID 83415, U.S.A.*

<sup>5</sup>*NRC “Kurchatov Institute”, ITEP, 117218 Moscow, Russia*

<sup>6</sup>*UCL, London WC1E 6BT, United Kingdom*

<sup>7</sup>*University of Manchester, Manchester M13 9PL, United Kingdom*

<sup>8</sup>*JINR, 141980 Dubna, Russia*

<sup>9</sup>*National Research Nuclear University MEPhI, 115409 Moscow, Russia*

<sup>10</sup>*CPPM, Université de Marseille, CNRS/IN2P3, F-13288 Marseille, France*

<sup>11</sup>*CENBG, Université de Bordeaux, CNRS/IN2P3, F-33175 Gradignan, France*

<sup>12</sup>*University of Texas at Austin, Austin, TX 78712, U.S.A.*

<sup>13</sup>*LPC Caen, ENSICAEN, Université de Caen, CNRS/IN2P3, F-14050 Caen, France*

<sup>14</sup>*LAPP, Université de Savoie, CNRS/IN2P3, F-74941 Annecy-le-Vieux, France*

<sup>15</sup>*Institute of Experimental and Applied Physics, Czech Technical University in Prague, CZ-12800 Prague, Czech Republic*

<sup>16</sup>*University of Warwick, Coventry CV4 7AL, United Kingdom*

<sup>17</sup>*Osaka University, 1-1 Machikaneyama Toyonaka, Osaka 560-0043, Japan*

<sup>18</sup>*Saga University, Saga 840-8502, Japan*

<sup>19</sup>*Laboratoire Souterrain de Modane, F-73500 Modane, France*

<sup>20</sup>*FMFI, Comenius Univ., SK-842 48 Bratislava, Slovakia*

<sup>21</sup>*LSCE, CNRS, F-91190 Gif-sur-Yvette, France*

<sup>22</sup>*Imperial College London, London SW7 2AZ, United Kingdom*

<sup>23</sup>*Institut Universitaire de France, F-75005 Paris, France*

<sup>24</sup>*Jyväskylä University, FIN-40351 Jyväskylä, Finland*

<sup>25</sup>*MHC, South Hadley, Massachusetts 01075, U.S.A.*

<sup>26</sup>*Institute for Nuclear Research, MSP 03680, Kyiv, Ukraine*

<sup>27</sup>*Charles University in Prague, Faculty of Mathematics and Physics, CZ-12116 Prague, Czech Republic*

(Dated: July 19, 2022)

The NEMO-3 experiment at the Modane Underground Laboratory has investigated the double- $\beta$  decay of  $^{48}\text{Ca}$ . Using 5.25 yr of data recorded with a 6.99 g sample of  $^{48}\text{Ca}$ , approximately 150 double- $\beta$  decay candidate events have been selected with a signal-to-background ratio greater than 3. The half-life for the two-neutrino double- $\beta$  decay of  $^{48}\text{Ca}$  has been measured to be  $T_{1/2}^{2\nu} = [6.4^{+0.7}_{-0.6}(\text{stat.})^{+1.2}_{-0.9}(\text{syst.})] \times 10^{19}$  yr. A search for neutrinoless double- $\beta$  decay of  $^{48}\text{Ca}$  yields a null result and a corresponding lower limit on the half-life is found to be  $T_{1/2}^{0\nu} > 2.0 \times 10^{22}$  yr at 90% confidence level, translating into an upper limit on the effective Majorana neutrino mass of  $\langle m_{\beta\beta} \rangle < 6.0 - 26$  eV, with the range reflecting different nuclear matrix element calculations. Limits are also set on models involving Majoron emission and right-handed currents.

PACS numbers: 23.40.-s; 14.60.Pq

\* Deceased

## I. INTRODUCTION

Neutrinoless double- $\beta$  decay ( $0\nu\beta\beta$ ) is the only feasible way of experimentally determining the Majorana or Dirac nature of light neutrinos. In the event that neutrinos are Majorana particles, this process may provide one of the most promising methods for measuring their absolute mass as well as the possible presence of additional CP-violating phases (see for example [1]). The corresponding two-neutrino decay mode ( $2\nu\beta\beta$ ) does not violate lepton number conservation and is allowed in the standard model. This mode has been observed for several isotopes and provides valuable inputs to nuclear matrix element (NME) calculations [2, 3]. However no clear evidence for  $0\nu\beta\beta$  has been established to date, with the best half-life limits in the range  $10^{24-25}$  yr [4–8].

$^{48}\text{Ca}$  is a particularly interesting nucleus with which to search for neutrinoless double- $\beta$  decay since it has the highest kinetic energy release  $Q_{\beta\beta} = (4267.98 \pm 0.32)$  keV of any known double- $\beta$  decaying isotope [9]. This  $Q_{\beta\beta}$ -value is significantly above the bulk of naturally occurring radioactive backgrounds and, moreover, ensures a favourable phase space which enhances the  $0\nu\beta\beta$  decay rate. However  $^{48}\text{Ca}$  has a low natural abundance of 0.187% and is difficult to enrich. Recent calculations also indicate a relative suppression of  $0\nu\beta\beta$  NMEs for  $^{48}\text{Ca}$  compared to other isotopes [10–16].

The  $2\nu\beta\beta$  decay mode of  $^{48}\text{Ca}$  was first discovered in the Hoover Dam TPC experiment, employing approximately 14 g of isotope [17]. With a sample of approximately 100 events, the half-life was measured to be  $T_{1/2}^{2\nu} = [4.3_{-1.1}^{+2.4}(\text{stat}) \pm 1.4(\text{syst})] \times 10^{19}$  yr. A subsequent measurement in the TGV planar germanium array experiment using 1 g of isotope yielded  $T_{1/2}^{2\nu} = 4.2_{-1.3}^{+3.3} \times 10^{19}$  yr based on only 5 events in the region of interest [18]. Both of these measurements are in agreement with the shell model prediction of  $T_{1/2}^{2\nu} = 3.7 \times 10^{19}$  yr [19]. Shell model calculations are expected to be the most reliable for  $^{48}\text{Ca}$ . Nevertheless recent predictions for the two-neutrino half-life span a range of  $(2.0 - 4.5) \times 10^{19}$  yr [20–23]. Other NME schemes are less well suited to this isotope, although there is a QRPA prediction of  $4.7 \times 10^{19}$  yr [24].

Searches for the  $0\nu\beta\beta$  decay of  $^{48}\text{Ca}$  began 60 years ago [25]. The main experimental technique that has been employed is the use of scintillating  $\text{CaF}_2$  crystals [26–28]. Such detectors have good energy resolution and detection efficiency in order to search for a line at  $Q_{\beta\beta}$ , while backgrounds generally prevent a straightforward measurement of the  $2\nu\beta\beta$  rate. No signals for  $0\nu\beta\beta$  have been found, with the best limit currently set by the ELEGANT VI experiment using 6.6 kg of  $\text{CaF}_2$  (7.6 g of  $^{48}\text{Ca}$ ) at  $T_{1/2}^{0\nu} > 5.8 \times 10^{22}$  yr at 90% C.L. [28].

## II. NEMO-3 DETECTOR

NEMO-3 is a tracking calorimeter detector, hosting several double- $\beta$  decaying isotopes in thin source foils arranged in a cylindrical geometry [29]. Electrons pass through 50 cm wide wire chambers on each side of the source foils, containing in total 6180 Geiger cells operating in a gas mixture comprising helium with 4% ethanol quencher, 1% argon and 0.15% water vapour. Surrounding the tracker is the calorimeter, consisting of 1940 plastic scintillators coupled to low radioactivity photomultipliers. A copper coil mounted outside the calorimeter generates a 25 G solenoidal magnetic field and beyond that 165 tons of iron, in addition to borated water, paraffin and wood, are used to shield the inner detector from external radioactivity. Approximately 95% of 1 MeV positrons are rejected by determining the track curvature, and 1 MeV electrons are measured in the calorimeter with an energy resolution (FWHM) ranging from 14.1% to 17.7% and a timing resolution  $\sigma_t \approx 250$  ps. A cylindrical coordinate system ( $R, \phi, Z$ ) is used, with the  $Z$ -axis pointing upwards, parallel to the source foil and tracker wires.

NEMO-3 hosts 6.91 kg of  $^{100}\text{Mo}$  and 0.93 kg of  $^{82}\text{Se}$ , as well as smaller amounts of  $^{96}\text{Zr}$ ,  $^{116}\text{Cd}$ ,  $^{130}\text{Te}$  and  $^{150}\text{Nd}$ . In all cases the experiment has made the most precise measurement of the  $2\nu\beta\beta$  half-life [2, 30–32]. The  $^{48}\text{Ca}$  source in NEMO-3 consists of 9 disks of  $\text{CaF}_2$  powder contained in thin ( $\approx 10 \mu\text{m}$ ) Teflon and polyethylene envelopes. Mylar foils, approximately  $20 \mu\text{m}$  thick, sandwich the disks on either side in order to hold them in place. The disks have a diameter of 46 mm and contain in total 17.5 g of  $\text{CaF}_2$ . With an enrichment fraction of  $(73.2 \pm 1.6)\%$ , this corresponds to 6.99 g of  $^{48}\text{Ca}$ . Figure 1 shows the vicinity of the  $^{48}\text{Ca}$  sources, imaged in single-electron events.

NEMO-3 ran from February 2003 until January 2011. A standard good-run requirement selects data-taking periods during which the detector was stable and the calorimeter was well calibrated. The resulting live-time is 5.25 yr, corresponding to a  $^{48}\text{Ca}$  exposure of  $36.7 \text{ g} \cdot \text{yr}$ .

## III. EVENT RECONSTRUCTION AND SELECTION

Readout of NEMO-3 is triggered by a calorimeter energy deposit of at least 150 keV in temporal and geometrical coincidence with a number of hits in the tracking detector, which has a negligible inefficiency for fiducial  $^{48}\text{Ca}$  two-electron ( $\beta\beta$ ) events. Offline, a tracking algorithm fits helices to clusters of Geiger cell hits, and performs additional fits to localise the origin of each track on the source foil and the entry point on the front face of the calorimeter. Isolated calorimeter hits that have no energy deposits in neighbouring calorimeter cells and that are matched to reconstructed tracks have their energies corrected for the track impact position and are stored as

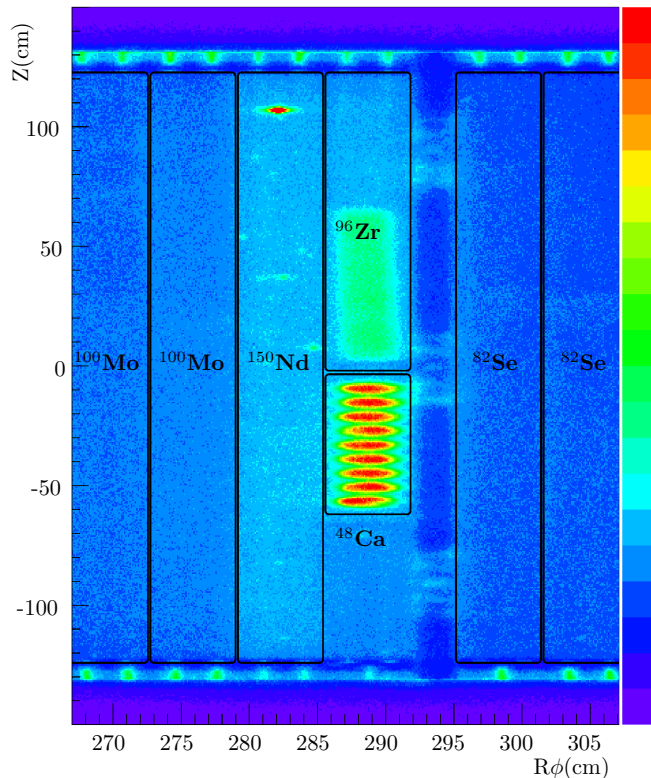


FIG. 1. An image of the NEMO-3 source foils in the vicinity of the  $^{48}\text{Ca}$  source, showing the rate of single-electron events (arbitrary scale) from the nine  $\text{CaF}_2$  disks mounted beneath the  $^{96}\text{Zr}$  source and next to the  $^{150}\text{Nd}$  source foil. The more distant  $^{82}\text{Se}$  and  $^{100}\text{Mo}$  sources do not contribute to backgrounds in the analysis of  $^{48}\text{Ca}$ . A copper tube forming part of the calibration system lies between the  $^{48}\text{Ca}/^{96}\text{Zr}$  sources and the  $^{82}\text{Se}$  foil.

electron candidates. For all event topologies containing a single electron, the sign of the track curvature is required to be consistent with a negatively charged particle.

Selected  $\beta\beta$  events must contain two electrons each with  $E_e > 400$  keV. The two tracks must intersect the  $^{48}\text{Ca}$  source strip and originate from the same point within tolerances  $|\Delta_{XY}| < 10$  cm and  $|\Delta_Z| < 15$  cm. In addition there must be no delayed  $\alpha$ -particle tracks, as defined in Section IV, in the event. The calorimeter times of the two electrons must be consistent with a common origin on the source foil and inconsistent with a crossing particle originating from outside the detector. No requirement is made on the number of additional calorimeter hits that may be present in the event.

Backgrounds are largely constrained in independent control samples. Common minimum electron and photon energy cuts of 400 keV ensure good agreement between data and Monte Carlo simulations across all the samples. Events containing single electrons (“1e”) are selected without the vertex and timing requirements described for  $\beta\beta$  events. Events containing a single electron

and a certain number of photons (“1eN $\gamma$ ”) do have similar timing requirements to  $\beta\beta$  events in order to eliminate crossing particles. Events that, by contrast, have timing characteristics consistent with particles crossing the detector, are used to constrain “external” backgrounds originating from outside the detector. Finally, “1e1 $\alpha$ ” events contain a single electron and delayed  $\alpha$ -particle consistent with  $^{214}\text{Bi} - ^{214}\text{Po}$  sequential decays.

The data are compared to simulated signal and background samples. In all cases the decays are generated using the DECAYO [33] program and passed through a detailed GEANT3 [34] based detector simulation, before being processed with the same reconstruction algorithms and event selection as the data.

#### IV. BACKGROUNDS AND CONTROL CHANNELS

Through interactions in or near the source foil,  $\beta$ -decaying isotopes or external  $\gamma$ -rays can give rise to events containing two electrons. Due to the high  $Q_{\beta\beta}$ -value of  $^{48}\text{Ca}$  very few isotopes form significant backgrounds in the vicinity of the  $0\nu\beta\beta$  signal. Backgrounds are classified as “internal” if they originate from the source foil itself and “external” if they originate from outside of the tracking volume. Radon progeny deposited on the source foil or nearby tracker wires form a third background category.

The  $^{48}\text{Ca}$  sources in NEMO-3 suffer from contamination by the chemically similar element strontium. Both  $^{90}\text{Y}$  and its parent  $^{90}\text{Sr}$ , with which it is in secular equilibrium, are essentially pure  $\beta$ -emitters and their activity is constrained predominantly by the measurement using the 1e channel, as shown in Fig. 2. The measured  $^{90}\text{Sr}/^{90}\text{Y}$  activity is observed to decrease with a half-life of  $(24.8 \pm 0.5)$  yr over the almost 8-year running period of the experiment. The discrepancy with the expected 28.8 yr half-life [35] corresponds to differences of (1 – 2)% between the measured and predicted distribution of  $^{90}\text{Sr}/^{90}\text{Y}$  background events across the lifetime of the experiment, due to imperfect modelling of the time dependence of the detector response. The resulting systematic uncertainty on the results presented here is negligible.

The external backgrounds indicated in Fig. 2 and elsewhere are modelled as combinations of  $^{228}\text{Ac}/^{212}\text{Bi}/^{208}\text{Tl}$ ,  $^{214}\text{Bi}$ ,  $^{60}\text{Co}$  and  $^{40}\text{K}$  in the photomultiplier tubes, scintillator blocks, iron structure and laboratory air surrounding the detector [36]. All of these components are allowed to vary from their central values in a fit to 1e and 1e1 $\gamma$  events that have a timing signature consistent with a particle of external origin passing through the  $^{48}\text{Ca}$  source. Due to detector inhomogeneities, the various external background components affecting the  $^{48}\text{Ca}$  analysis are found to differ from their detector-averaged levels by between –15% and +40%.

Events containing a gamma in addition to a single elec-

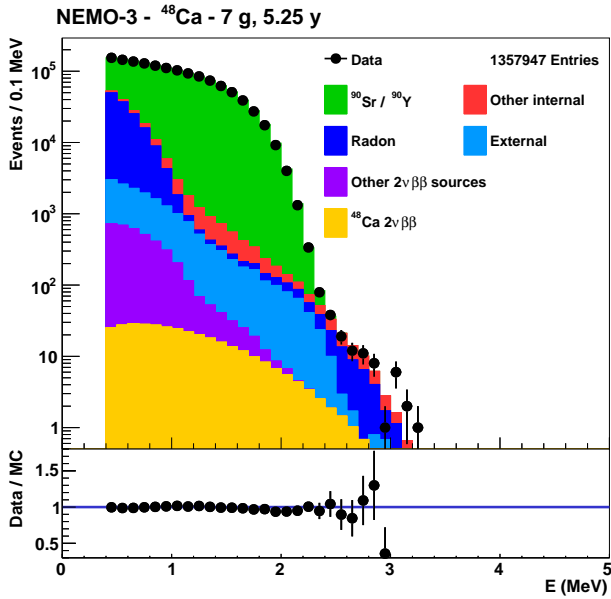


FIG. 2. The energy spectrum of electrons in events containing a single electron compared to the fitted background contributions (top panel) and as a ratio to the total Monte Carlo prediction (bottom panel). The dominant contribution is from  $^{90}\text{Sr}/^{90}\text{Y}$  with an end-point of 2.3 MeV. At higher energies the background from the radon daughter  $^{214}\text{Bi}$  becomes significant. There are sub-leading contributions from other internal backgrounds, external backgrounds and contamination of events from neighbouring source foils.

tron provide an additional control channel to constrain internal backgrounds such as  $^{208}\text{Tl}$ ,  $^{214}\text{Bi}$  and  $^{152}\text{Eu}$ . Figure 3 shows the sum of the electron and photon energies in  $1e1\gamma$  events. On top of a significant external background component, there is a contribution at low energies from  $^{90}\text{Sr}/^{90}\text{Y}$  decays in which the electron has undergone bremsstrahlung, with the other internal backgrounds constrained predominantly in the region  $E_{e+\gamma} \gtrsim 2.0$  MeV. The  $1e2\gamma$  events provide an additional statistically limited constraint, particularly on internal contamination by  $^{208}\text{Tl}$ .

The final background control sample consists of events containing a single electron and a delayed track consistent with being an  $\alpha$ -particle from  $^{214}\text{Bi} - ^{214}\text{Po}$  coincident decays. The minimum electron energy requirement is reduced to 200 keV in order to increase statistics, and  $\alpha$  tracks comprise one or more delayed hits in the vicinity of the electron vertex. The distribution of the  $\alpha$  track length in Fig. 4 shows a clear signal for radon progeny deposited on the surface of tracker wires close to the source foil, as well as a component deposited on the foil itself. Due to the small efficiency for  $\alpha$  particles generated in the  $\text{CaF}_2$  powder to reach the tracking volume, this channel does not constrain the internal  $^{214}\text{Bi}$  contamination of the isotope and provides only a weak signal for contamination inside the Mylar surrounding the source.

High-purity germanium (HPGe) measurements of the

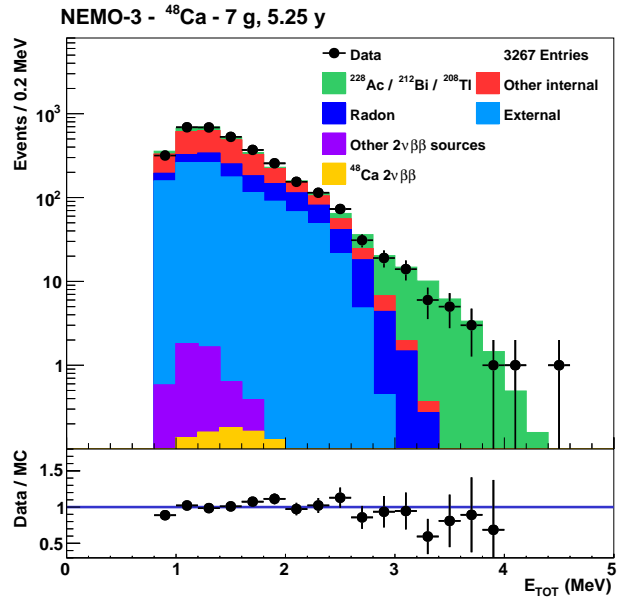


FIG. 3. The distribution of the total energy measured in events with one electron and one photon (top panel) and as a ratio to the total Monte Carlo prediction (bottom panel). The higher end of the distribution is dominated by the contribution due to the  $\beta$ -decay of  $^{208}\text{Tl}$  to  $^{208}\text{Pb}$  which always occurs with the emission of one or more photons, releasing a total energy of 5 MeV.

$^{48}\text{Ca}$  source disks were made following the dismantling of the NEMO-3 detector. Activities of  $^{152}\text{Eu}$  and  $^{40}\text{K}$  and upper limits on the activities of  $^{234m}\text{Pa}$  and  $^{228}\text{Ac}$  are derived and used as Gaussian constraints in the final background model.

A simultaneous binned log-likelihood fit is performed on all of the control samples discussed in Section III, as well as the HPGe constraints. In all cases the HPGe measurements are found not to be in significant tension with the NEMO-3 data. The resulting internal background activities are summarised in the first column of Table I.

## V. TWO NEUTRINO DOUBLE-BETA DECAY

Events containing exactly two electrons are selected with the requirements listed in Section III. The distribution of  $E_{\text{TOT}} = E_1 + E_2$  is shown in Fig. 5 along with the fitted backgrounds. The  $^{90}\text{Sr}/^{90}\text{Y}$  decays can give rise to two-electron events, for example through Møller scattering. The yield of events fitted in the  $\beta\beta$  sample alone and shown in Fig. 5 results in an activity for  $^{90}\text{Sr}/^{90}\text{Y}$  that is  $(9 \pm 4)\%$  higher than that measured in the single-electron control sample. Although not significant, this difference is considered as a source of systematic uncertainty.

The  $2\nu\beta\beta$  event yield is fitted in the high-energy region of the  $E_{\text{TOT}}$  distribution. An optimisation of the total (statistical plus systematic) uncertainty indicates

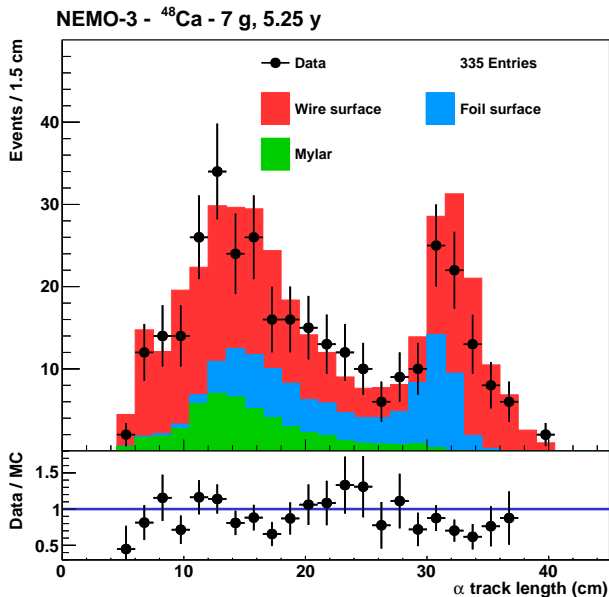


FIG. 4. The length of delayed tracks in  $1e1\alpha$  events, showing the contribution from radon progeny deposited on the wires of the tracking detector (red) and surface of the source foil (blue). A small contribution consistent with having an origin inside the Mylar surrounding the  $\text{CaF}_2$  disks, peaking at small track lengths, is also shown. The ratio of data events to the total Monte Carlo prediction is shown in the bottom panel.

an optimum requirement of  $E_{\text{TOT}} > 1.8 \text{ MeV}$ . Table I gives the fitted and observed event yield over the full range  $E_{\text{TOT}} > 0.8 \text{ MeV}$  and in the signal fit range  $E_{\text{TOT}} > 1.8 \text{ MeV}$ . In the fit range the number of signal events divided by the square root of the number of background events,  $S/\sqrt{B} \approx 23$ . The isotopes  $^{90}\text{Sr}/^{90}\text{Y}$  are the most important background. The fitted number of events  $N = 153$  and the selection efficiency calculated from Monte Carlo simulation,  $\epsilon = 3.1\%$ , correspond to a half-life given by:

$$T_{1/2} = \frac{\epsilon}{N} \cdot \frac{N_A m}{M} \cdot \ln(2) \cdot T,$$

where  $N_A$  is Avogadro's number,  $m$  is the mass of  $^{48}\text{Ca}$  with molar mass  $M$ , and  $T$  is the total exposure time.

In addition to the statistical uncertainty on the fitted number of signal events, the measurement of the two-neutrino half-life is subject to a number of systematic uncertainties, the majority of which relate to uncertainties in the modelling of signal and backgrounds. The discrepancy between the  $^{90}\text{Sr}/^{90}\text{Y}$  activity measured in the  $1e$  and  $2e$  samples is likely due to imperfect modelling of the mechanisms by which single  $\beta$ -electrons give rise to two-electron event signatures in the NEMO-3 detector. The central value for the  $^{48}\text{Ca}$   $2\nu\beta\beta$  half-life is obtained by fitting the  $^{90}\text{Sr}/^{90}\text{Y}$  activity simultaneously with the signal in the  $2e$  sample; constraining it to the activity measured in the  $1e$  sample gives rise to a change

between  $-2.4\%$  and  $+2.0\%$  in  $T_{1/2}^{2\nu}$ . Uncertainties in external and radon backgrounds give rise to changes in the measured half-life approximately one order of magnitude smaller than this.

The fractional uncertainty on the  $^{48}\text{Ca}$  enrichment fraction of 2.1% translates directly into a corresponding uncertainty on the measured two-neutrino half-life. Systematic uncertainties are also attributed to the source construction (diameter, thickness and material composition) as well as the precision ( $\approx 1^\circ$ ) with which the orientation of the  $^{48}\text{Ca}$  source strips is known within the NEMO-3 detector. Altogether these source construction uncertainties combine to give an asymmetric  $+3.7\%$  and  $-5.5\%$  uncertainty on the extracted  $2\nu\beta\beta$  half-life.

The largest systematic uncertainties relate to the detector response and calibration. A comparison of data and Monte Carlo simulations for dedicated  $^{207}\text{Bi}$  calibration runs indicates an uncertainty on the selection efficiency for double- $\beta$  decay topologies of  $\approx 7\%$  [7]. A calorimeter energy scale uncertainty of 1%, determined during dedicated scans of the calorimeter optical modules prior to construction and verified using in-situ calibration sources, translates into a 4.2% uncertainty on the  $2\nu\beta\beta$  activity. One of the most difficult distributions to simulate accurately is the opening angle of the two electrons in double- $\beta$  like event topologies, which requires accurate modelling not only of electron scattering in the source material but also the performance of the

Contribution	$A$ (mBq)	$N$	$N$ for $E_{\text{TOT}} > 1.8 \text{ MeV}$
$^{90}\text{Sr}/^{90}\text{Y}$ (in $\beta\beta$ )	$32.3 \pm 0.1$	997	32.1
$^{228}\text{Ac}/^{212}\text{Bi}/^{208}\text{Tl}$	$0.07 \pm 0.01$	6.8	1.5
$^{214}\text{Pb}/^{214}\text{Bi}$	$0.08 \pm 0.01$	12.9	3.8
$^{152}\text{Eu}$	$0.5 \pm 0.1$	0.13	–
$^{40}\text{K}$	$0.49 \pm 0.08$	0.27	–
$^{234m}\text{Pa}$	$0.3 \pm 0.1$	8.4	$1.6 \times 10^{-2}$
Non- $^{48}\text{Ca}$ Sources	–	16.0	3.1
External	–	7.6	0.81
Radon	–	7.9	2.9
Total Background	–	1057	44.2
$^{48}\text{Ca}$ $2\nu\beta\beta$	$(3.0 \pm 0.3) \times 10^{-2}$	302	153
Data	–	1368	192

TABLE I. Summary of the fitted internal background activities ( $A$ ), the expected number of background events ( $N$ ) from all sources, the fitted  $^{48}\text{Ca}$   $2\nu\beta\beta$  signal and the observed number of two-electron events. The numbers of events in the region  $E_{\text{TOT}} > 1.8 \text{ MeV}$ , in which the  $2\nu\beta\beta$  contribution has been fitted, are also given. Where multiple isotopes are listed on a single line then secular equilibrium is assumed. Note that for  $^{228}\text{Ac}/^{212}\text{Bi}/^{208}\text{Tl}$  the quoted activity is for  $^{228}\text{Ac}$  and the activity of  $^{208}\text{Tl}$  will therefore be smaller by a branching fraction of 35.9%. The uncertainties on the quoted activities are statistical only.

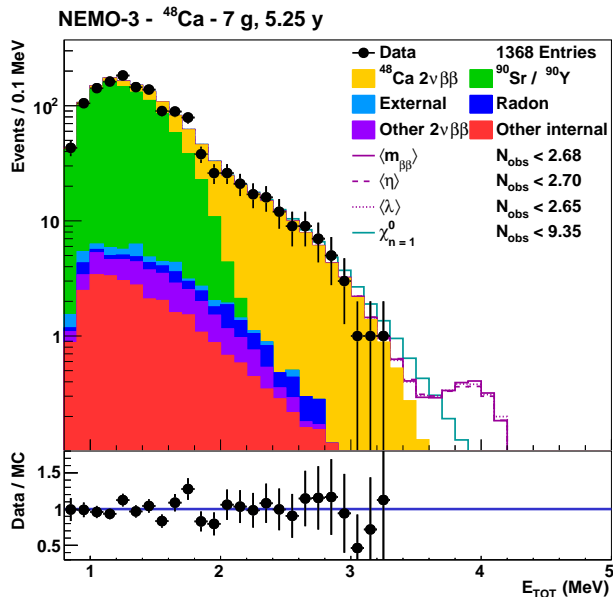


FIG. 5. The distribution of the summed electron energy in two-electron events. At low energies  $^{90}\text{Sr}/^{90}\text{Y}$  background events dominate, while other internal, external, radon and non- $^{48}\text{Ca}$  backgrounds are relatively small. The  $2\nu\beta\beta$ -signal is clearly visible at higher energies. Four open histograms represent limits on non-standard model double- $\beta$  decay processes, with 90% confidence level upper limits on the corresponding event yields  $N_{\text{obs}}$  also given. The ratio of data events to the total Monte Carlo prediction is shown in the bottom panel.

reconstruction algorithms for tracks with varying spatial separations. Separating two-electron events into exclusive samples comprising events with both electrons on the same side (SS) or opposite side (OS) of the source foil gives rise to fitted activities that are different from the combined sample by  $-14\%$  (SS) and  $+11\%$  (OS) respectively. Although this discrepancy has a statistical significance of only  $1.2\sigma$ , it is included here as an asymmetric systematic uncertainty on the half-life obtained from the inclusive  $2e$  sample.

For the source mass and exposure stated in Section II, the resulting half-life for the  $2\nu\beta\beta$  decay of  $^{48}\text{Ca}$  is:

$$T_{1/2}^{2\nu} = [6.4_{-0.6}^{+0.7}(\text{stat.})_{-0.9}^{+1.2}(\text{syst.})] \times 10^{19} \text{ yr},$$

where the systematic uncertainty is the sum in quadrature separately for upward and downward changes in the half-life of all the systematics described above and summarised in Table II.

## VI. NEUTRINOLESS DOUBLE-BETA DECAY

A search for neutrinoless modes of double- $\beta$  decay is performed on events selected with the criteria outlined in Section III, using the measurements of backgrounds and

the  $2\nu\beta\beta$  signal strength given in Sections IV and V, respectively. The main background for  $0\nu\beta\beta$  searches is the  $2\nu\beta\beta$  signal, which overlaps with the  $0\nu\beta\beta$  peak given the finite resolution of the calorimeter.

Four  $0\nu\beta\beta$  mechanisms are investigated in this work, where the decay proceeds via the exchange of light neutrinos, which largely shares its kinematics with  $R$ -parity violating ( $\hat{R}_p$ ) supersymmetric processes [37], through right-handed currents coupling right-handed quarks to right-handed leptons ( $\lambda$ ) and left-handed quarks to right-handed leptons ( $\eta$ ) [38], and with the emission of a single Majoron with spectral index  $n = 1$  [39].

Limits on the  $0\nu\beta\beta$  processes are obtained using a modified frequentist method based on a binned log-likelihood ratio test statistic ( $\text{CL}_s$ ) [40]. The statistic is calculated over the entire energy range above 0.8 MeV, with the background-only hypothesis providing a good fit to the data with an observed  $p$ -value ( $1-\text{CL}_b$ ) of 0.83.

The region above 3.4 MeV has the highest sensitivity to the  $0\nu\beta\beta$  peak. No events are observed in this window, illustrating the benefit of the high  $Q_{\beta\beta}$ -value of  $^{48}\text{Ca}$ , and a simple counting experiment limit obtained in this window is comparable to that obtained using the  $\text{CL}_s$  method over the larger energy range. Requiring a minimum energy of 3.6 MeV reduces the signal efficiency by a modest 15% while reducing the background expectation, dominated by  $2\nu\beta\beta$  events, to  $\approx 0.1$  events. This suggests the feasibility of background-free measurements with at least one order of magnitude longer exposures using the NEMO-3 technique.

When calculating the test statistic, the background and signal distributions are scaled by random factors drawn from Gaussian distributions with widths reflecting the uncertainties on the background normalisation and signal efficiency. An estimate of the effect of systematic uncertainties on the limit is thus included in the resulting distributions of the test statistic from which the confidence intervals are extracted. The estimate of the systematic uncertainty on the background model given in Section V is used, and the statistical uncertainty on the magnitude of the  $2\nu\beta\beta$  signal given in the same section

Origin	Uncertainty on $T_{1/2}^{2\nu}$
$^{90}\text{Sr}/^{90}\text{Y}$ background	[+2.0, -2.4]%
Other backgrounds	$\pm 0.3\%$
$^{48}\text{Ca}$ enrichment fraction	$\pm 2.1\%$
$^{48}\text{Ca}$ source construction	[+3.7, -5.5]%
Electron reconstruction efficiency	[+7.5, -6.5]%
Calorimeter energy scale	[+4.4, -4.0]%
Two-electron angular distribution	[+16, -10]%
Total	[+19, -14]%

TABLE II. Systematic uncertainties on the measured half-life for the  $2\nu\beta\beta$  decay of  $^{48}\text{Ca}$ .

is applied to that contribution. Both these uncertainties have negligible effects on the extracted limits, with the exception of the Majoron emission mode. The largest effect arises from the uncertainty on the signal efficiency. Given that the dominant contribution to the uncertainty on the  $2\nu\beta\beta$  efficiency is estimated from the data, which is not possible for the  $0\nu\beta\beta$  case, the uncertainty on the

latter signal efficiency is assumed to be equal in magnitude to the former.

The combined effect of the uncertainties outlined above on the limit placed on the light neutrino exchange  $0\nu\beta\beta$  process does not exceed 5%. The results of the limit-setting procedure are given in Table III and shown as open histograms in Fig. 5.

Mechanism	Efficiency (%)	$N^{\text{lim}}$ 90% C.L.		$T_{1/2}^{0\nu}$ 90% C.L. ( $10^{22}$ yr)	
		Expected	Observed	Expected	Observed
Light neutrino exchange / $\tilde{R}_p$ supersymmetry	16.9	< 2.67 – 3.15	< 2.68	> 1.71 – 2.02	> 2.02
Right-handed currents $\eta$	15.8	< 2.69 – 3.21	< 2.70	> 1.57 – 1.88	> 1.87
$\lambda$	9.91	< 2.65 – 3.07	< 2.65	> 1.03 – 1.20	> 1.19
Single Majoron emission ( $n = 1$ )	13.4	< 8.54 – 17.3	< 9.35	> 0.25 – 0.50	> 0.46

TABLE III. Limits on  $0\nu\beta\beta$  modes in  $^{48}\text{Ca}$  for  $E_{\text{TOT}} > 0.8\text{MeV}$ . The signal efficiencies and 90% C.L. upper limits on the number of events ( $N^{\text{lim}}$ ) are shown for the four investigated decay mechanisms. The limits expected given the background-only hypothesis are shown, with the ranges representing one standard deviation fluctuations of the background model and the systematic uncertainty on the signal efficiency.

The most stringent limit is obtained for the light Majorana neutrino exchange mechanism, where fewer than 2.68 events are observed at 90% C.L. With a signal detection efficiency of 16.9%, this corresponds to a lower limit of  $2.0 \times 10^{22}$  yr on the  $0\nu\beta\beta$  half-life. This result is within the range expected for the background-only hypothesis. As noted in the introduction, a search for the same process with scintillating  $\text{CaF}_2$  crystals has achieved a better limit of  $5.8 \times 10^{22}$  yr with roughly half of the exposure and a significantly higher efficiency [28].

The  $0\nu\beta\beta$  half-life lower limit can be converted into an upper limit on the effective Majorana neutrino mass  $\langle m_{\beta\beta} \rangle$ . Using the axial-vector coupling constant  $g_A = 1.27$ , the phase space factor from [41] and NMEs calculated in the shell model framework [11, 16] gives  $\langle m_{\beta\beta} \rangle < 16 - 24$  eV, whereas extending the NME selection to include calculations in the quasiparticle random-phase approximation (QRPA) [10, 13, 14], interacting boson model (IBM) [15] and energy density functional (EDF) [12] frameworks yields a wider range:  $\langle m_{\beta\beta} \rangle < 6.0 - 26$  eV.

In the context of supersymmetry, the same limit can be used to extract an upper limit on the  $\tilde{R}_p$  coupling constant  $\lambda'_{111}$ , assuming the decay proceeds via gluino exchange [37]. With the matrix elements given in [16, 42] a bound of  $\lambda'_{111} < (0.11 - 0.14) \times f$  is obtained on the coupling constant, with  $f = \left(\frac{m_{\tilde{g}}}{1\text{TeV}}\right)^2 \left(\frac{m_{\tilde{q}}}{1\text{TeV}}\right)^{1/2}$ , where  $m_{\tilde{q}}$  and  $m_{\tilde{g}}$  are the squark and gluino masses, respectively.

The existence of right-handed weak currents would lead to  $0\nu\beta\beta$  decays with different electron kinematics from the neutrino exchange mechanism. The summed energy spectra do not differ significantly from the light neutrino exchange mode, giving consistent limits on the number of observed events. However, the right-handed

modes have reduced detection efficiencies, particularly in the  $\lambda$  case, where there is a significant asymmetry in the energies of the two electrons. The resulting lower limits on the half-lives of these processes are  $1.9 \times 10^{22}$  yr and  $1.2 \times 10^{22}$  yr at 90% C.L. for the  $\eta$  and  $\lambda$  modes, respectively. These half-lives translate into upper bounds on the coupling constants of  $\langle \eta \rangle < (0.74 - 54) \times 10^{-7}$  and  $\langle \lambda \rangle < (7.6 - 47) \times 10^{-6}$ , using phase space factors and matrix elements from [43]. A unique strength of NEMO-like experiments is the ability to measure the kinematics of the individual electrons, which would allow for the distinction between right-handed currents and light neutrino exchange as the underlying mechanisms of  $0\nu\beta\beta$  in the event of a positive observation [38].

Lastly, a search is made for  $0\nu\beta\beta$  accompanied by the emission of a single Majoron. Models considered in the literature predict  $0\nu\beta\beta$  to occur with the emission of one or two Majorons, with the phase space factor  $G$  governed by  $G \propto (Q_{\beta\beta} - E_{\text{TOT}})^n$ , where  $n$  is the spectral index, commonly used to categorize decays arising from different models [39]. Decays with larger  $n$  (e.g. those with the emission of two Majorons) have broader summed energy spectra peaked at lower values and are thus more difficult to separate from the  $2\nu\beta\beta$  signal and other backgrounds. Given the relatively low statistics and high level of background at the lower end of the spectrum studied in this work, only the  $n = 1$  case is considered. The upper limit on the number of observed events is 9.35 at 90% C.L., which is combined with a detection efficiency of 13.4% to give a lower half-life limit of  $4.6 \times 10^{21}$  yr. This result improves on the previously published best limit of  $7.2 \times 10^{20}$  yr [44], obtained with data from [45]. An upper limit on the coupling between the  $\nu_e$  and the Majoron of  $\langle g_{ee} \rangle < (1.0 - 4.3) \times 10^{-4}$  is extracted from the half-life

limit using the phase space factor from [43] and matrix elements from [11–16].

## VII. SUMMARY AND CONCLUSIONS

The NEMO-3 experiment has investigated the double- $\beta$  decay of  $^{48}\text{Ca}$  with a small source comprising just 7g of isotope but with a total exposure time of more than 5 years. A larger and purer sample of  $\beta\beta$  events has been selected than in previous experiments and the half-life for the standard model two-neutrino double- $\beta$  decay mode has been measured to be  $T_{1/2}^{2\nu} = [6.4^{+0.7}(\text{stat.})_{-0.9}^{+1.2}(\text{syst.})] \times 10^{19}$  yr. This measured half-life is consistent with previous experimental measurements but has significantly smaller uncertainties. Note that this result differs from and supercedes a preliminary measurement of the  $2\nu\beta\beta$  half-life for  $^{48}\text{Ca}$  previously reported by the NEMO-3 collaboration [2, 3]. The change in reported half-life is due primarily to a modified description of the source geometry following the decommissioning of the NEMO-3 detector. The half-life reported in this work is longer than suggested by shell-model calculations, although the significance of this discrepancy is only at the level of  $2\sigma$ .

A search for  $0\nu\beta\beta$  decays of  $^{48}\text{Ca}$  has been performed

in the same dataset. No signal has been found, and a lower limit on the half-life for the light Majorana neutrino exchange mechanism for  $0\nu\beta\beta$  has been determined to be  $2.0 \times 10^{22}$  yr at 90% C.L. Limits have also been placed on  $\hat{R}_p$ -supersymmetry, right-handed currents and Majoron-emission models.

As expected for the high- $Q_{\beta\beta}$  isotope  $^{48}\text{Ca}$ , the region of interest for  $0\nu\beta\beta$  decays has a very low level of residual background arising almost entirely from the high-energy tail of the  $2\nu\beta\beta$  decay mode. Further investigation of the double- $\beta$  decay of  $^{48}\text{Ca}$  using a similar experimental technique but with larger exposures would therefore lead to improved limits on  $0\nu\beta\beta$  as well as provide a more precise measurement of the  $2\nu\beta\beta$  half-life. However, progress in the enrichment of  $^{48}\text{Ca}$  will be required for this to be experimentally feasible.

## ACKNOWLEDGMENTS

We thank the staff of the Modane Underground Laboratory for their technical assistance in running the experiment. We acknowledge support by the grants agencies of the Czech Republic, CNRS/IN2P3 in France, RFBR in Russia, STFC in the U.K. and NSF in the U.S.

- 
- [1] S. Pascoli, S. T. Petcov and T. Schwetz, Nucl. Phys. B **734** (2006) 24.
- [2] R. Saakyan, Ann. Rev. Nucl. Part. Sci. **63** (2013) 503.
- [3] A. S. Barabash, Nucl. Phys. A **935** (2015) 52.
- [4] K. Alfonso *et al.*, Phys. Rev. Lett. **115** (2015) 102502.
- [5] A. Gando *et al.*, Phys. Rev. Lett. **110** (2013) 062502.
- [6] M. Agostini *et al.*, Phys. Rev. Lett. **111** (2013) 122503.
- [7] R. Arnold *et al.*, Phys. Rev. D **89** (2014) 111101.
- [8] J. B. Albert *et al.*, Nature **510** (2014) 229.
- [9] A. A. Kwiatkowski *et al.*, Phys. Rev. C **89** (2014) 045502.
- [10] J. Suhonen, AIP Conf. Proc. **1488** (2012) 326.
- [11] E. Caurier *et al.*, Phys. Rev. Lett. **100** (2008) 052503.
- [12] T. R. Rodriguez and G. Martinez-Pinedo, Phys. Rev. Lett. **105** (2010) 252503.
- [13] J. Suhonen, J. Phys. G **19** (1993) 139.
- [14] F. Šimkovic *et al.*, Phys. Rev. C **87** (2013) 045501.
- [15] J. Barea, J. Kotila and F. Iachello, Phys. Rev. C **91** (2015) 034304.
- [16] M. Horoi, Phys. Rev. C **87** (2013) 014320.
- [17] A. Balysh *et al.*, Phys. Rev. Lett. **77** (1996) 5186.
- [18] V. B. Brudanin *et al.*, Phys. Lett. B **495** (2000) 63.
- [19] E. Caurier *et al.*, Phys. Rev. C **50** (1994) 225.
- [20] E. Caurier, F. Nowacki and A. Poves, Phys. Lett. B **711** (2012) 62.
- [21] M. Horoi, S. Stoica and B. A. Brown, Phys. Rev. C **75** (2007) 034303.
- [22] L. Zhao, B. A. Brown and W. A. Richter, Phys. Rev. C **42** (1990) 1120.
- [23] Y. Iwata *et al.* JPS Conf. Proc. **6** (2015) 030057.
- [24] C. M. Raduta, A. A. Raduta and I. I. Ursu, Phys. Rev. C **84** (2011) 064322.
- [25] J. McCarthy, Phys. Rev. **97** (1955) 1234.
- [26] E. der Mateosian and M. Goldhaber, Phys. Rev. **146** (1966) 810.
- [27] K. You *et al.*, Phys. Lett. B **265** (1991) 53.
- [28] S. Umehara *et al.*, Phys. Rev. C **78** (2008) 058501.
- [29] R. Arnold *et al.*, Nucl. Instrum. Meth. A **536** (2005) 79.
- [30] J. Argyriades *et al.*, Phys. Rev. C **80** (2009) 032501.
- [31] J. Argyriades *et al.*, Nucl. Phys. A **847** (2010) 168.
- [32] R. Arnold *et al.*, Phys. Rev. Lett. **107** (2011) 062504.
- [33] O. A. Ponkratenko, V. I. Tretyak and Y. G. Zdesenko, Phys. Atom. Nucl. **63** (2000) 1282.
- [34] GEANT Detector Description and Simulation Tool, CERN Program Library Long Writeup W5013 (1995).
- [35] E. Browne, Nuclear Data Sheets 82 (1997) 379.
- [36] J. Argyriades *et al.*, Nucl. Instrum. Meth. A **606** (2009) 449.
- [37] J. D. Vergados, H. Ejiri and F. Šimkovic, Rep. Prog. Phys. **75** (2012) 106301.
- [38] R. Arnold *et al.*, Eur. Phys. J. C **70** (2010) 927.
- [39] P. Bamert, C. P. Burgess and R. N. Mohapatra, Nucl. Phys. B **449** (1995) 25.
- [40] T. Junk, Nucl. Inst. Meth. A **434** (1999) 435.
- [41] J. Kotila and F. Iachello, Phys. Rev. C **85** (2012) 034316.
- [42] A. Wodecki, W. A. Kamiński and F. Šimkovic, Phys. Rev. D **60** (1999) 115007.
- [43] J. Suhonen and O. Civitarese, Phys. Rept. **300** (1998) 123.
- [44] A. S. Barabash, Phys. Lett. B **216** (1989) 257.
- [45] R. K. Bardin *et al.*, Nucl. Phys. A **158** (1970) 337.